Image Quality Improvement via Spatial Deconvolution in Optical Tomography : Time-Series Images

Yong Xu[1,2], Yaling Pei[2], Harry L. Graber[1,2], and Randall L. Barbour[1,2]

[1]SUNY Downstate Medical Center and [2]NIRx Medical Technologies, LLC.

INTRODUCTION

Image quality is one of key factors that determines the practicality of an imaging scheme. Experience with diffuse optical tomography (DOT) research and applications has indicated that most image reconstruction algorithms yield blurred images because localized information from the object domain is mapped to more than one position in the image domain. To reduce the blurring in reconstructed images and improve image quality, as measured by parameters such as quantitative spatial and temporal accuracy of recovered optical coefficients, a linear deconvolution strategy was proposed [1,2]. An illustration depicting this strategy is shown in Figure 1. As shown in the figure, the function of the deconvolution operator/filter is to reduce the mixing of information and to make the recovered image as nearly as possible a one-to-one correspondence between object and image pixels. The original idea of the deconvolution scheme is to borrow the concept of frequency encoding of spatial information from MR imaging and to use this strategy to label information that is "transferred" from the object to image space[3]. As discussed below, in practice we find that the method works best when applied in time domain directly, rather than in the frequency domain [1].

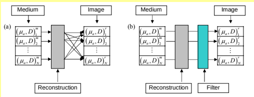

Figure 1. Panel A, schematic depicting the action of typical DOT image reconstruction algorithm, which yields blurred images because information from each object domain location is mapped to more than one position in the image domain. Panel B, the action of an ideal image-correcting filter, which is to counteract the information spreading aspect of the reconstruction algorithm's action.

In this report, we continue our investigation of image quality improvement via the spatial deconvolution scheme in DOT. In contrast to our previous work[2,4], in which we have demonstrated that the deconvolution method brings about substantial qualitative improvement in spatial resolution and spatial accuracy for 2D[4] and 3D[2] static images reconstructed from steady-state (cw) DOT measurement data, we now investigate the effect of the spatial deconvolution method on the dynamical features of time-series images[5,6] in dense-scattering media by quantitative assessments of spatial and temporal accuracy of the reconstructed images.

METHODS

2.1 Spatial Deconvolution Algorithm

The reasoning that underlay our linear deconvolution strategy, and the mathematical details of its implementation, are given in Refs. 1, 2 and 4. Here, we only briefly introduce the method in an intuitive way which is compared to the procedure of calibration of a measurement system.

We know that no measurement system is perfect. It is necessary to calibrate the system before measurement. As shown in Figure 2(a), calibration of a measurement system can be represented by the equation:

$$[S_0] = [c][S_m],$$

where $[S_0]$ and $[S_m]$ denote a series of standard signals and the corresponding measured signals, respectively, and $[c]$ are calibration coefficients. After the calibration, the measured data can be corrected by the calibration coefficients $[c]$ to acquire accurate measurements.

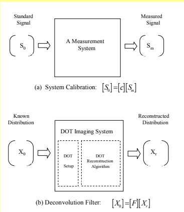

Figure 2. Analogy between the calibration of a measurement system and the deconvolution scheme.

Similarly, for DOT imaging system, as shown in Figure 2(b), we also need to calibrate before reconstruction. Suppose the optical coefficient distribution $[\mathbf{X}_0(\mathbf{r})]$ in the spatial domain under consideration is known:

$$[\mathbf{X}_0(\mathbf{r})] = [x_{01}, x_{02}, \ldots, x_{0n}]^T,$$

where the distribution $[\mathbf{X}_0(\mathbf{r})]$ is discretized by an *n*-node mesh for numerical computations. Taking the known distribution as the input for the imaging system, we can obtain the reconstructed distribution

$$[\mathbf{X}_r(\mathbf{r})] = [x_{r1}, x_{r2}, \ldots, x_{rn}]^T.$$

So calibration of the imaging system can be performed by computing $[\mathbf{X}_0(\mathbf{r})] = [F]\,[\mathbf{X}_r(\mathbf{r})]$, where the calibration coefficient $[F]$ is an $n \times n$ matrix and is called deconvolution operator or image-correcting filter. In practice, the basic steps to generate an image-correcting filter are as follows:

(1) Generate *N* independently known optical coefficient distributions by computer:

$$\left[\mathbf{X}_0^{(i)}(\mathbf{r})\right] = \left[x_{01}^{(i)}, x_{02}^{(i)}, \cdots, x_{0n}^{(i)}\right]^T \qquad i = 1, 2, \cdots, N$$

where $N \geq n$;

(2) Use the forward model [7,8] to simulate the detector readings from the known distributions;

(3) Reconstruct the optical coefficient distributions from the simulated detector readings by use of the inverse model:

$$\left[\mathbf{X}_r^{(i)}(\mathbf{r})\right] = \left[x_{r1}^{(i)}, x_{r2}^{(i)}, \cdots, x_{rn}^{(i)}\right]^T \qquad i = 1, 2, \cdots, N$$

(4) Solve the matrix equation to determine the image-correcting filter:

$$\begin{bmatrix} x_{01}^{(1)} & x_{01}^{(2)} & \cdots & x_{01}^{(N)} \\ x_{02}^{(1)} & x_{02}^{(2)} & \cdots & x_{02}^{(N)} \\ \vdots & \vdots & \ddots & \vdots \\ x_{0n}^{(1)} & x_{0n}^{(2)} & \cdots & x_{0n}^{(N)} \end{bmatrix} = \begin{bmatrix} f_{11} & f_{12} & \cdots & f_{1n} \\ f_{21} & f_{22} & \cdots & f_{2n} \\ \vdots & \vdots & \ddots & \vdots \\ f_{n1} & f_{n2} & \cdots & f_{nn} \end{bmatrix} \begin{bmatrix} x_{r1}^{(1)} & x_{r1}^{(2)} & \cdots & x_{r1}^{(N)} \\ x_{r2}^{(1)} & x_{r2}^{(2)} & \cdots & x_{r2}^{(N)} \\ \vdots & \vdots & \ddots & \vdots \\ x_{rn}^{(1)} & x_{rn}^{(2)} & \cdots & x_{rn}^{(N)} \end{bmatrix}$$

Finally, any image $[\mathbf{Y}_r(\mathbf{r})]$ that is recovered using the same numerical mesh and source-detector geometry as used in the generation of filter $[F]$ can be corrected by computing the matrix product $[F][\mathbf{Y}_r(\mathbf{r})]$.

The test medium geometry and source-detector configuration used for the filter generation and image reconstructions that are reported here are shown in Figure 3. For all computations considered in this report, the absorption coefficient of the test medium's background is μ_a=0.06 cm^{-1}, and the medium has spatially homogeneous and temporally invariant scattering, with μ_s=10 cm^{-1}.

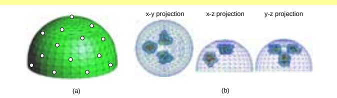

Figure 3: 3D FEM mesh, source-detector configuration and heterogeneous test medium. (a) The hemispheric mesh has 982 nodes, 4309 tetrahedral elements and a diameter of 8 cm, where 25 sources and 29 detectors are marked with small white circles. (b) The heterogeneous test medium in the projection planes shows the positions and shapes of three inclusions, which is used in demonstrations of the efficacy of deconvolution at improving reconstructed image accuracy.

2.2 Dynamic features of inclusions

To explore dynamic characteristics of time-series images under deconvolution operation, as shown in Figure 4, the following four time-varying functions are assigned to the absorption coefficients of the test medium's inclusions:

(a) sinusoidal time series:

$$\mu_a(t) = \mu_{a0} + \Delta\mu_a \cos(2\pi f_0 t + \varphi_0) \tag{1}$$

(b) amplitude-modulated time series:

$$\mu_a(t) = \mu_{a0} + \Delta\mu_a\left[1 + 0.5\sin(2\pi f_a t + \varphi_a)\right]\cos(2\pi f_0 t + \varphi_0) \tag{2}$$

(c) constant-amplitude time series with time-dependent frequency:

$$\mu_a(t) = \mu_{a0} + \Delta\mu_a \cos\left\{2\pi f_0\left[1 - 0.5\sin(2\pi f_m t + \varphi_m)\right]t + \varphi_0\right\} \tag{3}$$

(d) time series with time-dependent frequency and amplitude modulation:

$$\mu_a(t) = \mu_{a0} + \Delta\mu_a\left[1 + 0.5\sin(2\pi f_a t + \varphi_a)\right]\cos\left\{2\pi f_0\left[1 - 0.5\sin(2\pi f_m t + \varphi_m)\right]t + \varphi_0\right\} \tag{4}$$

Where parameters μ_{a0}=0.12 cm^{-1}, $\Delta\mu_a$=0.024 cm-1, f_0=0.1 Hz, f_a=0.03 Hz, f_m=0.03 Hz, φ_0=0, φ_a=0 and φ_m=0 have been used for the calculation of time-series curves in Figure 4.

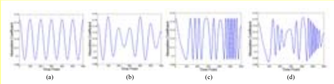

Figure 4: Time series assigned to the optical coefficients of the test medium's inclusions: (a) sinusoidal time series; (b) amplitude-modulated time series; (c) frequency-modulated time series; (d) amplitude and frequency-modulated time series, where the four time-series curves correspond to Eqs. (1)-(4), respectively.

2.3 3D Detector Noise Model

In most demonstrated cases of this report the white Gaussian noise is added to simulated detector readings for investigating the robustness of our deconvolution method. The noise-to-signal ratio of our 3D detector noise model can be expressed by[9]

$$\sigma_{ij} = \left(\frac{N}{S}\right)_{ij} = K_0 + \left(K_w - K_0\right)\left(\frac{d_{ij}}{W}\right)^4 \tag{5}$$

where d_{ij} is the distance between the i-th source and the j-th detector; W is the maximal distance between sources and detectors, i.e. W=max(d_{ij}); K_0 is the noise-to-signal ratio at the co-located point of source and detector; and K_w stands for the noise-to-signal ratio when the distance between source and detector equals W. This noise model is in agreement with usual experimental and clinical expeirence.

To quantitatively analyze the effect of noise on spatial and temporal accuracy of reconstructed images, we, here, define six noise levels:

Level 1: K_0=0.5% and K_w=5%;
Level 2: K_0=1% and K_w=10%;
Level 3: K_0=2% and K_w=20%;
Level 4: K_0=3% and K_w=30%;
Level 5: K_0=4% and K_w=40%;
Level 6: K_0=5% and K_w=50%.

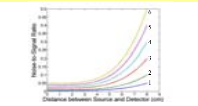

Figure 5: Variation in noise-signal (N/S) ratio with distance between source and detector locations: the N/S ratio increased with the distance is described by Eq. (5), which is in agreement with usual experimental and clinical experiences, where curves 1-6 correspond to the six noise levels defined in section 2.3, respectively.

Figure 5 shows the source-detector distance dependence of the noise-to-signal ratios of these six noise levels. In next section we will illustrate the spatial and temporal accuracy of images on the six noise levels.

2.4 Quantitative Assessments of Spatial and Temporal Accuracy

In this report, we select the spatial and temporal correlations between target medium and reconstructed images as the measurements of spatial and temporal accuracy of recovered images, respectively, for whose numerical values can be precisely evaluated[9].

The spatial correlation is defined as

$$c(t_0)_{uv} = \frac{1}{N_d - 1}\sum_{i=1}^{N_d}\left(\frac{u_i - \overline{u}}{s_u}\right)\left(\frac{v_i - \overline{v}}{s_v}\right) \tag{6}$$

Where $u_i = u(x_i, y_i; t_0)$ is accurate values, $v_i = v(x_i, y_i; t_0)$ is reconstructed values, $\overline{u}$ and $\overline{v}$ are the mean values of u and v, and s_u and s_v are their standard deviations. The sum runs over all (N_d) mesh nodes.

The temporal correlation is defined as

$$c(x_0, y_0)_{uv} = \frac{1}{N_t - 1}\sum_{i=1}^{N_t}\left(\frac{u_i - \overline{u}}{s_u}\right)\left(\frac{v_i - \overline{v}}{s_v}\right) \tag{7}$$

Where $u_i = u(x_0, y_0; t_i)$ is accurate values, $v_i = v(x_0, y_0; t_i)$ is reconstructed values, and the sum runs over all (N_t) time points.

RESULTS

Qualitative and quantitative assessments of the effectiveness of the linear deconvolution method when applied to time series of images are presented in this section. In the first example, in which noise-free data were used, a comparison between convolved and deconvolved images, for selected time frames within the image sequence, are shown in Figure 6. These results demonstrate that the spatial accuracy of the images is markedly improved by use of the linear deconvolution correction, and that there is no comcomitant degradation of temporal information. An important, logical next step is to determine the effect of noise in the detector data on the spatial and temporal accuracy. Figure 7 shows a case with added noise, in which the level-2 white Gaussian noise is added to detector measurements. Comparing Figures 7(a) and 7(b), it can be seen that using deconvolution the spatial accuracy of time-series images is improved, but the temporal accuracy of the images is degraded due to the additive detector noise. However, when a simple temporal low-pass filter is used to denoise the deconvolved time-series images, the quality of the images is additionally enhanced, as shown in Figure 7(c). In next three cases, we have investigated three simple denoising techniques: temporal low-pass filtering, spatial low-pass filtering and optimizing regularization factors. The corresponding results of reconstructed images are presented in Figures 8, 9 and 10, respectively. These results show that the three simple denoising methods can all enhance the performance of deconvolution. To quantitatively assess the spatial and temporal accuracy of reconstructed time-series images, we make use of definitions (6) and (7) to calculate the spatial and temporal correlations of reconstructed images under different conditions. The contrast dependence of spatial correlations of recovered images with two different noise levels is shown in Figure 11. Figure 12 gives the noise dependence of spatial correlations of reconstructed results. The quantitative results indicate that the spatial accuracy is clearly improved by deconvolution, even for high noise levels. The amplitude dependence and noise dependence of temporal correlations of reconstructed time-series images are plotted in Figures 13 and 14, respectively. Figures 13 and 14 show that the temporal accuracy increases with the increase in amplitude of time series and is degraded by the deconvolution procedure. Finally, the comparisons of temporal correlations of time-series images between four different dynamic features of inclusions are listed in Table 1, which clearly indicates that simple time series is easier to recover than complex time series.

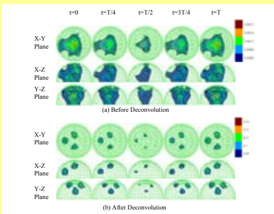

Figure 6: Reconstructed time-series images of three-inclusion hemispheric test medium without noise added to the detector readings: (a) uncorrected images at five time points within a period; (b) deconvolved images, where a sinusoidal time series as shown in Fig. 3(a) is assigned to the absorption coefficients of three inclusions. Numbers along color bar give the quantitative values of the spatially varying μ_a and the period (T) is 10 seconds.

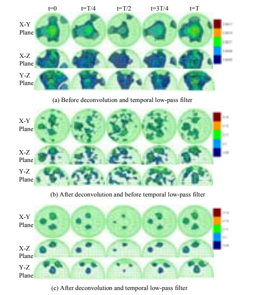

Figure 7: Reconstructed time-series images with level-2 noise added to the detector readings: (a) uncorrected images at five time points within a period; (b) deconvolved images without temporal low-pass filtering; (c) deconvolved images with temporal low-pass filtering, where a sinusoidal time series as shown in Fig. 4(a) is assigned to the absorption coefficients of three inclusions. Numbers along color bar give the quantitative values of the spatially varying μ_a and the period (T) is 10 seconds.

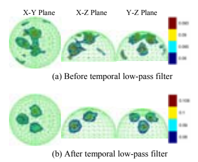

Figure 8: Reconstructed image denoised by a temporal low-pass filter. (a) deconvolved image before low-pass filter; (b) deconvolved image after low-pass filter. Where the noise level is K_0=1% and K_w=5%, absorption contrast of inclusion is 2, and Regularization factor λ=1.0.

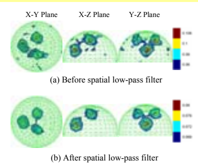

Figure 9: Reconstructed image denoised by a spatial low-pass filter. (a) deconvolved image denoised by temporal low-pass filter but before spatial low-pass filter; (b) deconvolved image after temporal and spatial low-pass filters. Where the noise level is K_0=5% and K_w=10%, absorption contrast of inclusion is 2, and regularization factor λ=1.0.

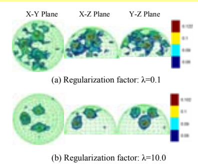

Figure 10: Reconstructed image denoised by optimizing regularization factors. (a) deconvolved image denoised by temporal low-pass filter, λ=1.0 ; (b) deconvolved image denoised by temporal low-pass filter, λ=10.0. Where the noise level is K_0=5% and K_w=10%, absorption contrast of inclusion is 2.

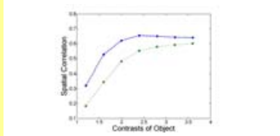

Figure 11: Contrast dependence of spatial accuracy of deconvolved images denoised by temporal low-pass filter. The blue curve corresponds to level-2 noise; green curve level-3 noise.

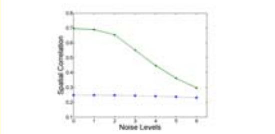

Figure 12: Noise dependence of spatial accuracy of reconstructed images denoised by temporal low-pass filter. The blue curve corresponds to undeconvolved values; green curve deconvolved values. The absorption contrast is 2.4.

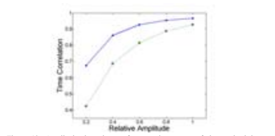

Figure 13: Amplitude dependence of temporal accuracy of deconvolved images denoised by temporal low-pass filter. The blue curve corresponds to level-2 noise; green curve level-3 noise. Time-averaged contrast is 2.

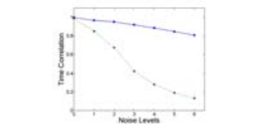

Figure 14: Noise dependence of temporal accuracy of reconstructed images denoised by temporal low-pass filter. The blue curve corresponds to undeconvolved values; green curve deconvolved values. Time-averaged contrast is 2 and the relative amplitude is 0.2.

Table 1: Time correlations in different dynamical features of objects (Noise: K_0=1%, K_w=10%)

Dynamic Features	Without Low-pass Filter		With Temporal Low-pass Filter	
	Before Deconv.	After Deconv.	Before Deconv.	After Deconv.
1	0.8231	0.2478	0.9522	0.6729
2	0.8352	0.2680	0.9548	0.6928
3	0.8172	0.2476	0.6966	0.4244
4	0.8332	0.2692	0.7685	0.5200

CONCLUSIONS

In this report, we have investigated effectiveness of the linear deconvolution method applied to reconstructed time-series images. The qualitative and quantitative results show that

(1) For noise-free or low noise level (<0.5%) data, both spatial and temporal accuracy of time-series images are markedly improved by the deconvolution method;
(2) Simple time-series features (e.g. sinusoidal) are easier to recover than complex time-series features (e.g. modulation of frequency);
(3) For noisy data, deconvolution procedures can significantly improve the spatial accuracy of time series images but degrade the temporal accuracy;
(4) Denoising methods (even simple techniques) can enhance the performance of the deconvolution method;
(5) Combined with a temporal low-pass filter, satisfactory spatial and temporal accuracy (>60%) can be achieved by use of the deconvolution method at an experimental noise level (K_0=1% and K_w=10%).

REFERENCES

1. R. L. Barbour, H. L. Graber, Y. Xu, Y. Pei, R. Aronson, "Strategies for imaging diffusing media," Transport Theory and Statistical Physics, in press
2. H. L. Graber, Y. Xu, Y. Pei, and R. L. Barbour, "Qualitative and quantitative improvement of optical tomographic reconstructed images via spatial deconvolution: three-dimensional case," Applied Optics, in review
3. H. L. Graber, R. L. Barbour, and Y. Pei, "Quantification and enhancement of image reconstruction accuracy by frequency encoding of spatial information," in OSA Biomedical Topical Meetings, OSA Technical Digest (Optical Society of America, Washington DC, 2002), pp. 635–637.
4. Y. Xu, H. L. Graber, Y. Pei, and R. L. Barbour, "Improved accuracy of reconstructed diffuse optical tomographic images via spatial deconvolution: 2D quantitative characterization," Applied Optics, in review
5. R. L. Barbour, H. L. Graber, Y. Pei, S. Zhong, and C. H. Schmitz, "Optical tomographic imaging of dynamic features of dense-scattering media," J. Optical Society of America A 18:3018-3036 (2001).
6. H. L. Graber, Y. Pei, R. L. Barbour, "Imaging of spatiotemporal coincident states by DC optical tomography," IEEE Transactions on Medical Imaging 21:852-866 (2002).
7. Y. Pei, Y. Pei, H. L. Graber, and R. L. Barbour, "Normalized-constraint algorithm for minimizing inter-parameter crosstalk in DC optical tomography," *Optics Express* **9**, 97–109 (2001).
8. Y. Pei, H. L. Graber, and R. L. Barbour, "Influence of systematic errors in reference states on image quality and on stability of derived information for DC optical imaging," *Applied Optics* **40**, 5755–5769 (2001).
9. H. L. Graber, Y. Pei, R. L. Barbour, D. K. Johnston, Y. Zheng, and J. E. Mayhew, "Signal source separation and localization in the analysis of dynamic near–infrared optical tomographic time series," in *Optical Tomography and Spectroscopy of Tissue V (Proceedings of SPIE, Vol. 4955)*, B. Chance, R. R. Alfano, B. J. Tromberg, M. Tamura, E. M. Sevick-Muraca, Eds., pp. 31–51 (2003).

ACKNOWLEDGEMENT

This research was support in part by the National Institutes of Health (NIH) under Grants R21-HL67387, R21-DK63692, R41-CA96102 and R43-NS49734, and by the US Army under Grant DAMD017-03-C-0018.

I look to ***THE DIFFUSION OF LIGHT*** and education as the resource to be relied on for ameliorating the condition, promoting the virtue, and advancing the happiness of man.

— Thomas Jefferson (1822)